



The Influence of Sealing Processes and Machining Operations on the Scratch and Wear Resistance of Anodized AlSi9Cu3(Fe) Diecasting Alloy

GIULIA SCAMPONE ^{1,2} and GIULIO TIMELLI¹

1.—Department of Management and Engineering, University of Padova, Stradella S. Nicola, 3, 36100 Vicenza, Italy. 2.—e-mail: giulia.scampone@phd.unipd.it

The effects of hydrothermal and cold sealing processes on the scratch and wear resistance of the anodic layer have been studied. High-pressure diecast AlSi9Cu3(Fe) alloy plates were anodized in a sulfuric acid electrolyte at 16°C and further sealed in boiled water or in a NiF₂ solution at 25°C. To analyze the influence of pre-anodizing machining operations, the plates were studied in the as-diecast condition and after milling. Metallographic investigations and image analysis techniques were carried out to study the morphology and thickness of the anodic layer. Hardness, wear, and scratch measurements were also performed to characterize the surface mechanical properties. The results showed that the sealing processes enhanced the wear and scratch resistance of the anodized surfaces because of the precipitation of hydrates that sealed the surface porosity. The thicker oxide layer formed on the milled substrate led to a greater wear resistance compared to the as-diecast surface, owing to reduced wear of the underlying aluminum substrate. Finally, a cracked mechanically mixed layer, which was enriched with fragmented intermetallics and anodic layer debris, was formed on the anodized surfaces at the end of the wear tests.

INTRODUCTION

Aluminum-silicon (Al-Si) foundry alloys are commonly used for many applications, especially in the automotive sector, where excellent castability and a favorable combination of good mechanical properties and low density are essential features to produce high-performance industrial components.¹ To electrically insulate the castings and increase their surface mechanical properties, an anodizing process can be performed.^{2–5} In this process, the aluminum component is the anode of an electrolytic cell, and the growth of a surface layer of aluminum oxide is promoted by the action of the electrical current.^{2,5} Even though this process is widely performed in wrought Al alloys, Al-Si foundry alloys are still challenging to anodize. The high number of

alloying elements present in the foundry alloys makes the substrate electrochemically heterogeneous and limits the growth of the oxide film.⁷

The further enhancement of the corrosion resistance of an anodized surface can be achieved by performing a sealing process. During this treatment, the seal chemistry interacts with the anodic structure forming reaction products that either precipitate or are adsorbed within the oxide structure. The microporosity of the anodic layer is thus sealed, preventing the further penetration of aggressive agents.⁸ Even though various types of seal chemistry can be used to obtain different surface requirements,^{9–11} the most diffused processes are hydrothermal sealing and cold sealing based on a nickel fluoride solution.

In hydrothermal sealing (HTS), the anodized component is immersed in boiling deionized water for a time of about 2 min/ μm thickness.⁸ During the early stages of HTS, the sealing solution enters the pores and initiates the dissolution of the porous structure. This promotes the precipitation of small,

dispersed flakes of hydrated alumina (i.e., boehmite) within the pores and on the top surface of the anodic layer.¹² Over time, the precipitation of boehmite flakes increases in both quantity and size, forming a densely intertwined structure within the porous structure. Once a saturation condition is achieved within the pores, large flakes of boehmite begin to grow vertically on the top surface. Ono et al.¹² reported that at the end of the sealing process, a three-layered structure is formed. This structure consists of an outer layer of coarse and flaky boehmite, an intermediate layer where boehmite precipitates into a densely intertwined structure, and an inner part where the pores are filled with boehmite.¹² Lopez et al.¹³ described how the precipitation of bayerite, a trihydrate stable at room temperature, also contributed to the occlusion of the porous structure. The volumetric expansion associated with the conversion of anodic alumina to aluminum hydroxides leads to the formation of a more compact and denser anodic layer, improving the corrosion resistance after hydrothermal sealing. However, due to the softer nature of these hydroxides compared to anodic alumina, a decrease in the surface hardness and abrasion resistance may occur.⁸

Even though the HTS is a sustainable process, it is a very slow treatment with high industrial cost. Therefore, in the 1980 s, the cold sealing process based on nickel fluoride solutions (CS-NF) was developed.¹⁴ The fluoride ions present in the sealant solution have a great affinity to aluminum ions, allowing for a reduction in the temperature of the sealing bath.¹⁵ In this process, the fluoride ions penetrate the pores and trigger an exchange mechanism that alters the local pH, promoting the reaction between the nickel ions and the oxide structure. Nickel hydroxide precipitates within the pores, occluding them. Aluminum hydroxides also precipitate, even after the end of the sealing process. Kalantary et al.¹⁵ referred to this phenomenon as the second stage of the aging process, which involves the hydration of the anodic layer due to exposure to atmospheric humidity.

Due to the key role of the sealing processes, many patents have been developed. Some of them are focused on the addition of specific reagents (e.g., a combination of rare-earth metal and oxidizing agents,¹⁶ a metal salt-free agent,¹⁷ and a nickel-free reagent¹⁸), while other patents refer to the steps and times of the sealing process.^{18,19} However, these works and patents are mainly focused on wrought Al alloys.

Concerning the sealing of Al-Si alloys, a limited number of studies have been developed.^{20,21} Mohe-dano et al.²⁰ investigated the influence of different sealing processes on AlSi7Mg0.3 alloys. The analyzed sealants were based on salts of cerium, cobalt, nickel, potassium permanganate, and orthophosphoric acid. Zhu et al.²¹ studied how the HTS promotes the cracking of the anodic layer, and this

behavior was attributed to the intrinsic residual stresses developed when the porous aluminum oxide is transformed into boehmite.

Due to the importance of producing high-resistant anodized Al-Si castings, further analyses are required to comprehend how different sealing processes affect the surface mechanical properties of anodized Al-Si alloys. This research focuses on examining the impact of HTS and CS-NF sealing on the surface hardness, wear, and scratch resistance of a diecast AlSi9Cu3(Fe) alloy. The effects of anodizing and sealing processes on both as-diecast and milled surfaces have been investigated.

EXPERIMENTAL PROCEDURE

Casting Process and Machining Operations

In the present work, an AlSi9Cu(3)Fe alloy (EN AB-46000²²) was selected to produce high-pressure diecast plates. Commercial ingots were melted inside a 300-kg crucible in a gas-fired furnace set up at $690 \pm 5^\circ\text{C}$. The chemical composition is given in Table S-I (refer to online supplementary material). The casting was carried out using a cold-chamber diecasting machine with a locking force of 2.9 MN. A more detailed description of the diecasting machine, the casting procedure, and the process parameters is given elsewhere.^{23,24}

Before analysis, the plates were stored at room temperature for at least 5 months, similar to a T1 condition. Generally, T1 temper designation is used for components that are cooled from an elevated temperature shaping process and then naturally aged.²²

To analyze the impact of milling operations on the growth of the oxide layer, a set of plates was studied in as-diecast condition, while another one was mechanically milled over one side to a final thickness of 4.5 ± 0.1 mm. The machining operation was carried out using a Dahly CNC machining center equipped with a movable table. The milling process was designed to reduce the material thickness by 1.5 mm, which was achieved through three consecutive passes removing 0.8 mm, 0.5 mm, and finally 0.2 mm, respectively. The operation was performed at a tool rotational speed of 2000 rpm. This process allowed the removal of the positive surface segregation,²⁵ thereby exposing a substrate with a coarser microstructure and lower amounts of eutectic and intermetallic compounds to anodizing.

Anodizing and Sealing Parameters

The plates were preliminary treated in a water solution of H_2SO_4 and H_2O_2 with a concentration of 80 g/L for 1 min to degrease and clean the surface. According to industrial practice, the specimens were anodized under galvanostatic conditions inside a water solution of 160 g/L H_2SO_4 at $16 \pm 3^\circ\text{C}$.²⁵ The DC electric current density was linearly increased

from 0 A/dm² to 0.74 A/dm² in 10 min and then held constant at 0.74 A/dm² for 35 min.

Two different types of sealing processes were performed:

- a hydrothermal sealing in demineralized water at 95 ± 5°C for 30 min;
- a cold sealing in a 5 g/L NiF₂ water solution at room temperature for 10 min.

A schematic representation of the manufacturing procedure, as well as the evolution of the surface appearance during the different steps of the process, are shown in Figs. S-1 and S-2, respectively (refer to online supplementary material).

Microstructural Characterization

Samples for microstructural analysis were drawn from the cross-section of plates and mechanically prepared to a 3- μ m finish with diamond paste and polished with a commercial silica colloidal suspension. The microstructural observations were carried out using an optical microscope (OM, LeicaTM DM6 M) and a field emission gun scanning electron microscope (FEG-SEM, FEI QuantaTM 250) operating at 10 kV and equipped with an energy dispersive spectrometer (EDS, EDAXTM).

A detailed characterization of the untreated substrates was carried out. At least 30 contiguous micrographs, each with an area of 240 × 170 μ m², were collected along the casting surface. Secondary dendrite arms spacing (SDAS) was measured by applying the line intercept method,²⁶ and the area fraction occupied by Fe- and Cu-rich compounds was quantified by using an image analyzer. To easily detect the Fe-rich compounds, the polished samples were etched in a 20% H₂SO₄ water solution at 70°C. A chemical etching in a 25% HNO₃ aqueous solution at 70°C was instead carried out on the polished samples to highlight the Cu-rich compounds. The quantification of the eutectic fraction was performed after chemical etching in a modified Murakami solution (60 mL H₂O, 5 g K₃Fe(CN)₆, and 10 g NaOH).

The thickness of the anodic oxide layer was measured in the anodized plates according to the EN ISO 1463:2004 standard. About 10 micrographs of 240 × 170 μ m² were collected along the casting surface, and at least five measurements were performed for each frame.

X-ray diffraction (XRD) measurements were also performed on the top surface of the sealed samples to identify the phases formed during the sealing process. To focus the analysis on the oxide layer, the diffraction patterns were obtained in the 2 θ degree range of 5°–55° with a step size of 0.01°, using an Xpert MPD diffractometer (PANalyticalTM) with Mo K α radiation at 40 kV and 30 mA.

The surface roughness parameters Ra and Rz were evaluated by using a Taylor Hobson Surtronic 3 + stylus profilometer. The instrument had a

resolution of 0.01 μ m, and at least eight measurements were performed for each condition with a sampling length of 8 mm.

Wear, Microhardness, and Scratch Tests

For wear testing, 40-mm-diameter discs were drawn from the central zone of the plates. A TRB tribometer (CSM InstrumentsTM) was used to perform wear tests with a ball-on-disc configuration. An Al₂O₃ ball of 6 mm diameter was used as counter body, and a load of 2 N was applied. Dry sliding tests were conducted in an air atmosphere at room temperature (25 ± 5°C) and humidity of 10–15%.

The sliding speed was set constant at 0.06 m/s for a distance of 163 m; the test time was about 45 min. At least three tests were performed for each condition.

The wear rate (ω) was calculated as

$$\omega = \frac{V}{L \times N} \quad (1)$$

where V is the wear volume, L is the sliding distance, and N is the applied load.

After each test, the profile and the area of the wear track were measured by using the profilometer. The wear volume (V) was calculated as the average wear area integrated over the perimeter (p) of the circular track ($p = 2\pi r$, with $r = 5.2$ mm).

During the tests, both the anodic layer and the substrate wore out. Thus, the wear resistance of the entire “anodic film + aluminum substrate” system was investigated.

Vickers microhardness measurements were carried out with an FM-810 microhardness tester (Future-TechTM). The indentations were performed in the cross-section of the anodic layer according to the ASTM E384-17 standard. Due to the reduced thickness of the oxide layer in the as-diecast substrates, the microhardness measurements were only performed in the anodized milled substrates. At least ten measurements were carried out for each plate by applying a load of 0.05 kg_f and a dwell time of 10 s.

Scratch tests were performed at room temperature with a Hardness Test Pen according to EN ISO 22557:2020. This standard specifies a method for determining the resistance of a coating to scratches introduced by a usually hand-held loaded stylus.²⁷ The applied load ranged from 0 N to 30 N and was applied gradually until the critical load was reached, i.e., the load required to scratch the oxide layer and expose the substrate.

RESULTS AND DISCUSSION

Characterization of the Substrate

The microstructure of the diecast AlSi9Cu3(Fe) alloy mainly consisted of primary α -Al less-branched dendrites and an Al-Si eutectic structure (Fig. 1). The high cooling rate and the great amount of Cu

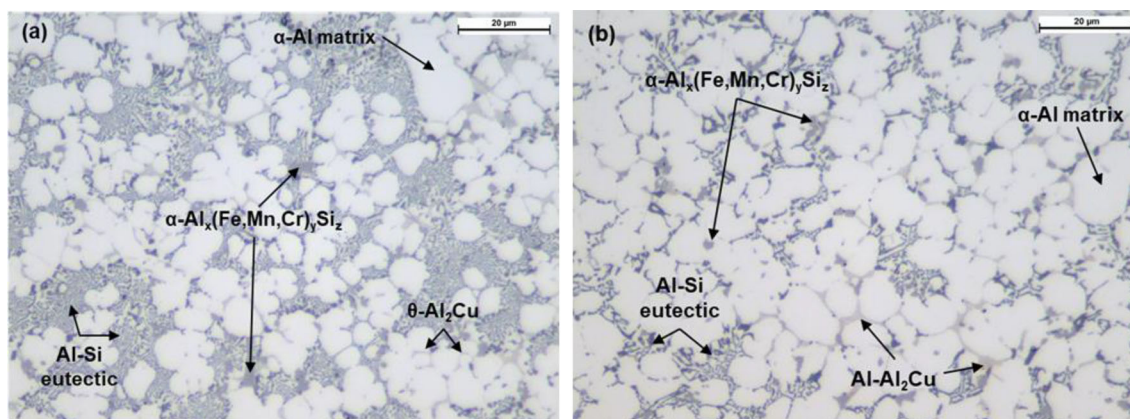


Fig. 1. Typical microstructures of diecast AlSi9Cu3(Fe) alloy. The micrographs refer to the (a) as-diecast and (b) milled substrates.

prevented the coarsening of the Si particles, which appeared with a fibrous, fine morphology and an average size of about 1 μm . Fe- and Cu-rich intermetallics were also observed in the interdendritic channels and at the grain boundaries. The Fe-rich compounds were identified as blocky-like $\alpha\text{-Al}_x(\text{Fe,Mn,Cr})_y\text{Si}_z$ particles, while the Cu-bearing particles were present as $\theta\text{-Al}_2\text{Cu}$ phase in the form of pockets of fine eutectic (Al + Al₂Cu) or blocky-like Al₂Cu particles. Even though these phases were present in both as-diecast and milled substrates, the fraction and distribution strictly depended on the finishing condition. The chemical composition, measured on the investigated substrates by optical emission spectrometry, is given in Table S-II of the supplementary material.

The as-diecast substrate showed greater concentrations of many alloying elements, especially Si, Fe, and Cu. This resulted in a greater fraction of eutectic structure and Fe- and Cu-rich intermetallics. As shown in Fig. 2, the eutectic fraction varied from $41 \pm 3\%$ to $39 \pm 2\%$ in the as-diecast and milled substrates, respectively. A similar trend was observed about the Fe- and Cu-rich compounds.

The microstructural variations between the investigated substrates were attributed to the milling operation. The Al-Si die castings present generally a positive surface macrosegregation, i.e., higher solute content than the surrounding, which results from a combination of inverse segregation and exudation during the casting process.²⁸ This segregated surface zone has a limited thickness ($250 \pm 60 \mu\text{m}$ ²⁴); thus, it was removed by the surface milling operations. Contrarily, the as-diecast substrate showed higher concentrations of eutectic Si-, Fe-, and Cu-rich intermetallics due to the presence of surface macrosegregation. Similar results were obtained by Caliarì et al.²⁹

Characterization of the Anodic Layer

Figure 3 shows the anodic layer formed on the as-diecast and milled substrates. A thin, continuous, and well-bounded oxide film was grown in the as-

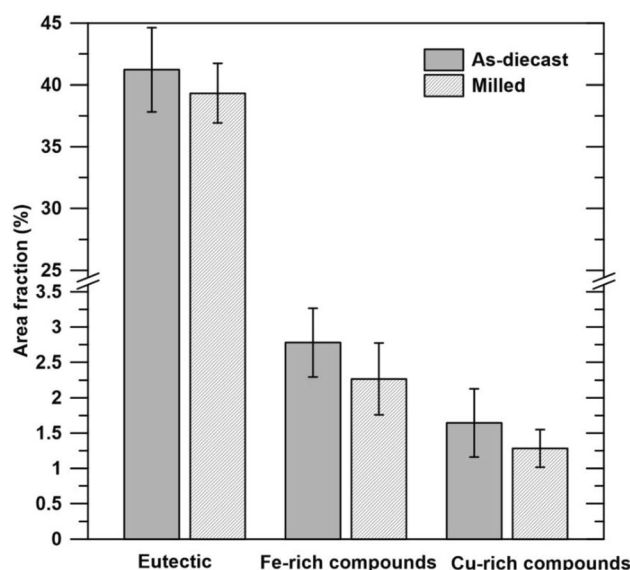


Fig. 2. Mean eutectic fraction and area fraction of the Fe- and Cu-rich intermetallics in the as-diecast and milled substrates.

diecast AlSi9Cu3(Fe) alloy plates, while a thicker layer with a scalloped oxide/metal interface was formed on the milled substrate. The differences in the thickness and morphology of the oxide layer can be attributed to two main factors that alter the electrochemical potential of the surface, i.e., the different surface topography and the microstructural variation of the substrate. Concerning the surface topography, surface irregularities such as burrs, machining marks, or asperities formed during blasting are sites for the charge concentration and inhibit the formation of the anodic layer. This phenomenon is known as the concentration polarization effect.² The diecast surface exhibited a rougher surface with numerous burrs generated during the diecasting process because of the use of a partially worn die (refer to Figs. S-2 and S-4 in the supplementary material). Conversely, the milled surface was smoother, facilitating a more uniform distribution of electrical charge during anodizing

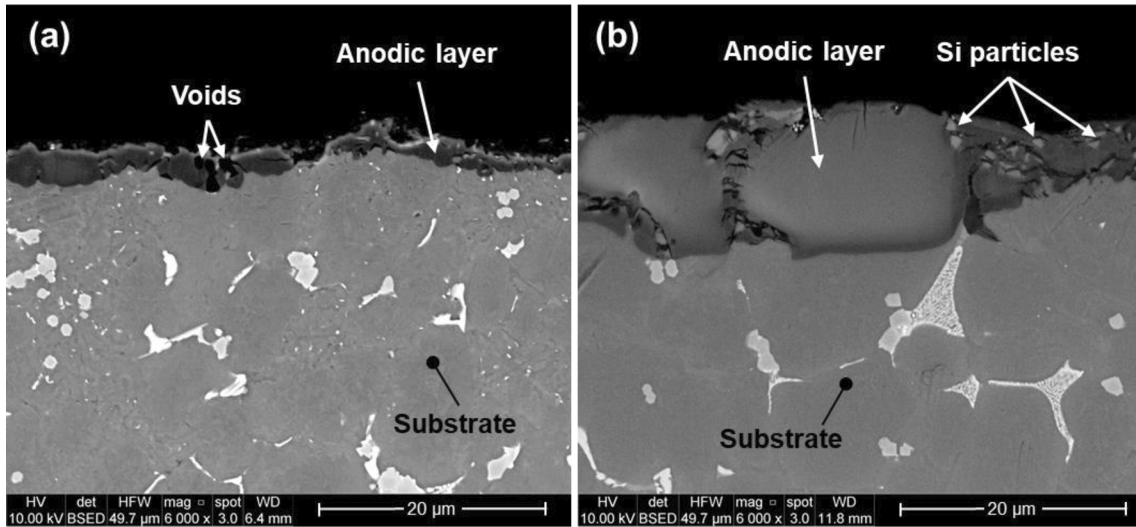


Fig. 3. FEG-SEM micrographs of the anodic oxide layer formed on the (a) as-diecast and (b) milled substrates.

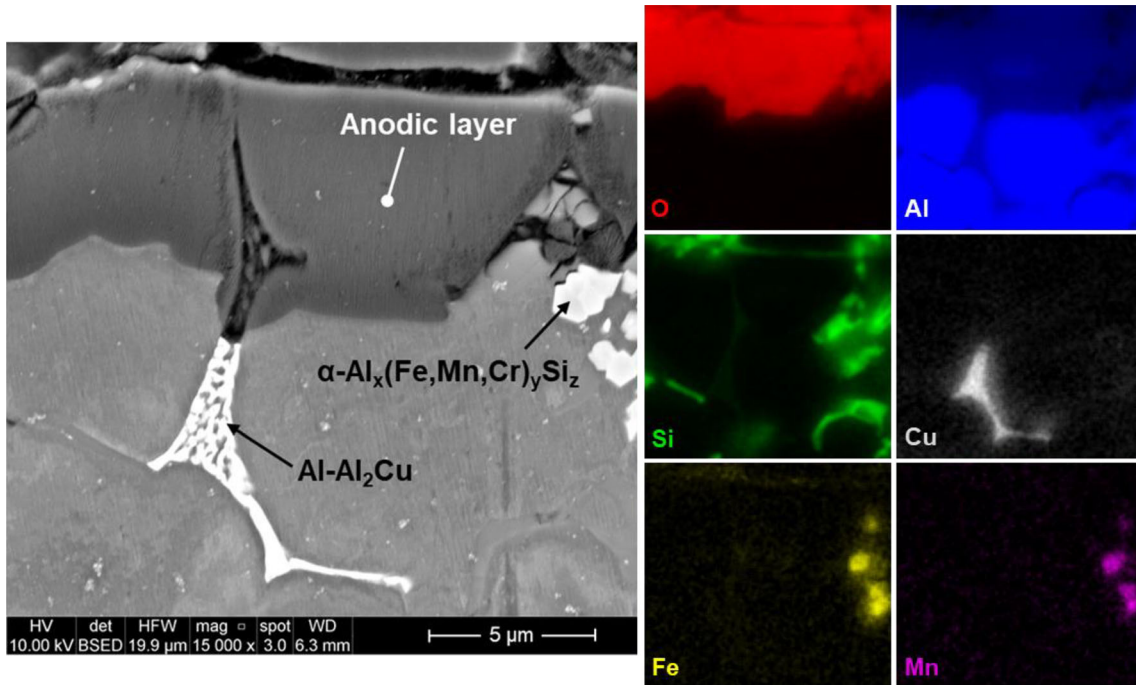


Fig. 4. FEG-SEM micrograph and EDS mapping showing the interaction of $\alpha\text{-Al}_x(\text{Fe,Mn,Cr})_y\text{Si}_z$ and $\text{Al-Al}_2\text{Cu}$ phases with the growth of the anodic layer.

and thereby promoting the thickening of the anodic layer. Similarly, the greater eutectic fraction present on the as-diecast surface hindered the thickening of the anodic layer, while the larger quantity of coarser $\alpha\text{-Al}$ phase on the milled surface facilitated the propagation of the oxidation front during anodizing. Further details concerning the impact of Al-Si microstructure on the growth and morphology of the anodic layer can be found elsewhere.⁷

The presence of Si particles, $\alpha\text{-Al}_x(\text{Fe,Mn,Cr})_y\text{Si}_z$ compounds, and the Al_2Cu phase contributed to making the investigated surfaces electrochemically

heterogeneous during anodizing. The EDS mapping illustrated in Fig. 4 shows the impact of these phases on the growth of the anodic layer.

On both as-diecast and milled substrates, the eutectic Si particles exhibited a compact shape with reduced size (see Fig. 1), enabling their embedding within the anodic layer. This is consistent with other findings reported in the literature,^{21,30} which indicate that Si particles $< 5 \mu\text{m}$ do not adversely impact the continuity of the anodic layer. Otherwise, the Al_2Cu phase was oxidized and dissolved during the anodizing process, as evidenced by the

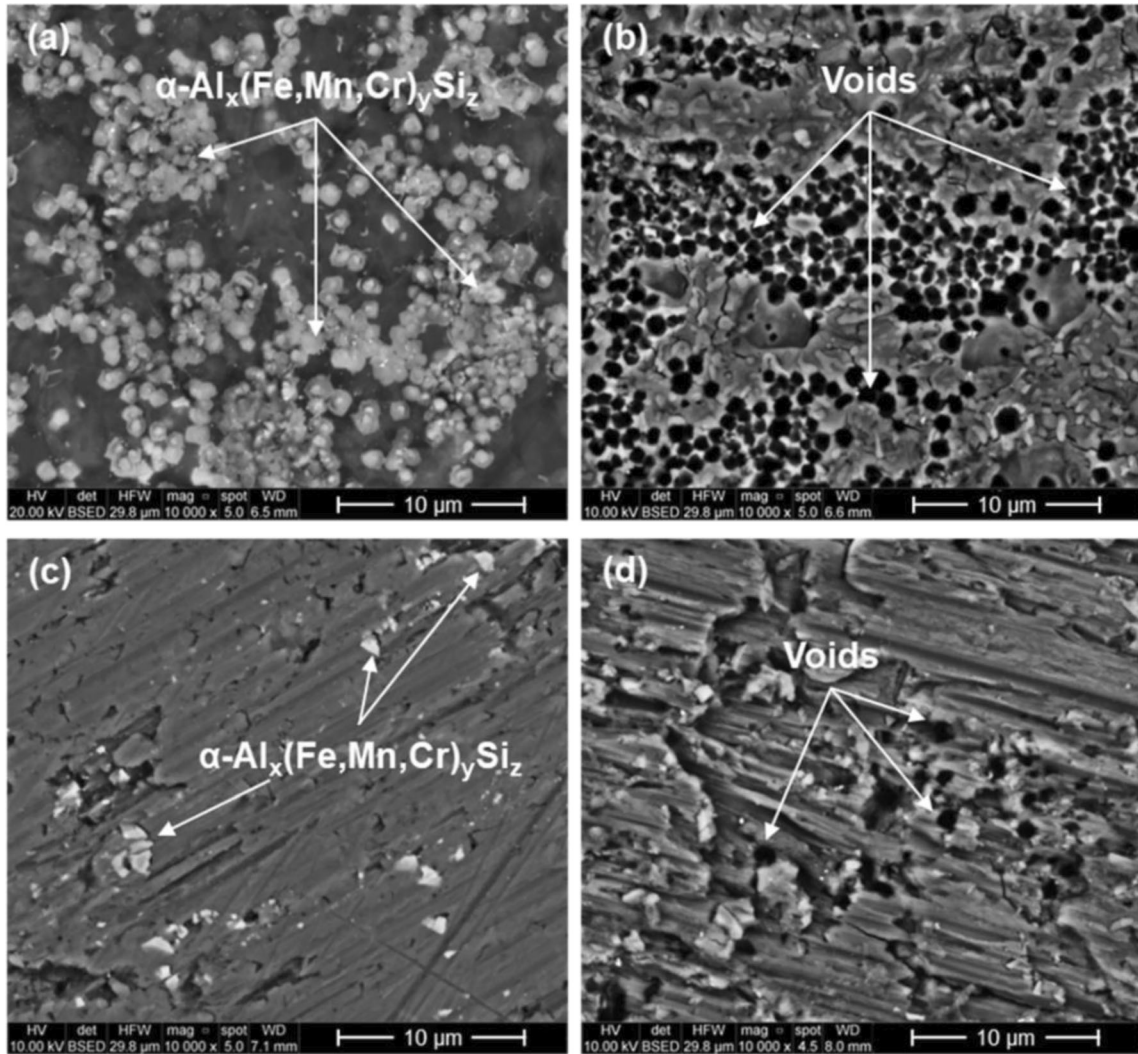


Fig. 5. FEG-SEM micrographs of the top view of the (a, b) as-diecast and (c, d) milled plates (a, c) before and (b, d) after the anodizing process.

absence of Cu in concomitance with the anodized Al_2Cu compound in the EDS mapping of Fig. 4. Similar findings were reported by Fratila-Apachitei et al. in Ref. 31. No large voids or pores were detected because of the dissolution of this phase.

Contrarily, the anodizing of $\alpha\text{-Al}_x(\text{Fe,Mn,Cr})_y\text{Si}_z$ intermetallics led to the formation of numerous voids in the oxide layer because of the dissolution of this phase.^{31,32} Figure 5 shows the top views of the as-diecast and milled plates before and after the anodizing process.

Due to the presence of surface macrosegregation (see in “Characterization of the Substrate” section), the as-diecast substrate showed a large amount of $\alpha\text{-Al}_x(\text{Fe,Mn,Cr})_y\text{Si}_z$ phase, while the milled substrate exhibited fewer Fe-rich particles with a fragmented morphology because of milling operations. This resulted in a higher surface porosity on the as-diecast surface after the anodizing process. In fact, the porosity’s area fraction was approximately 12% and 2% in the as-diecast and milled substrate,

respectively. During the sealing process, this surface porosity was partially plugged because of the precipitation of hydrates.

To investigate the precipitated phases, XRD measurements were carried out on the top surface of the sealed plates, and the software X’Pert HighScore Plus (PANalyticalTM) was used to identify the peaks. The diffraction pattern reported in Fig. 6 shows that Al, Al_2O_3 , $\text{Al}(\text{OH})_3$, and $\text{AlO}(\text{OH})$ phases were present in all the sealed samples. The aluminum substrate had a cubic structure, as confirmed by the correspondence of the peaks with the standard ones (JCPDS card no. 00-004-0787). The anodizing process led to the formation of a tetragonal Al_2O_3 phase (JCPDS card no. 00-046-1131), in agreement with the findings of Ilango et al.³³ Differently from the face-centered cubic (FCC) Al phase, which is renowned for its exceptional combination of high strength and significant ductility, the tetragonal Al_2O_3 phase is primarily recognized for its high hardness, electrical insulation properties,

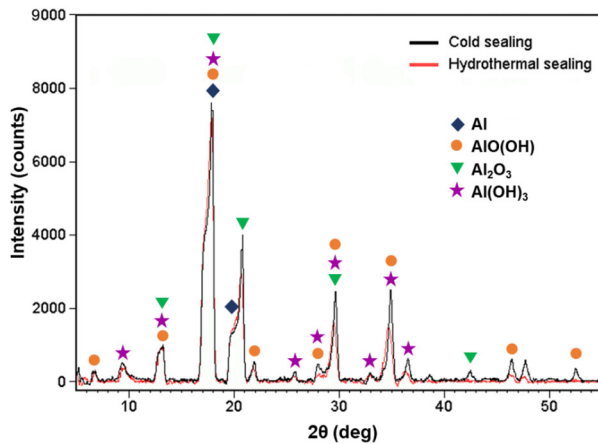


Fig. 6. XRD spectra of the cold-sealed and hydrothermal-sealed samples.

and elevated melting point. The increased hardness of the Al_2O_3 structure contributes to enhancing the surface mechanical properties of the casting after anodizing, especially the wear resistance (a more detailed description will be presented in the following sections).

Orthorhombic boehmite, $\text{AlO}(\text{OH})$, peaks and monoclinic bayerite, $\text{Al}(\text{OH})_3$, peaks were also observed in both hydrothermal-sealed and cold-sealed samples (JCPDS cards no. 00-021-1307 and 00-020-0011) in agreement with other results reported in the literature.^{13,34} The sealing process was governed by the dissolution/hydration reaction that occurred within the pores and on the outer surface of the anodic layer. When the sealing solution came into contact with the anodic structure, the pore walls and the surface of the anodic layer dissolved, allowing the subsequent precipitation of aluminum hydroxides in the form of boehmite and bayerite.^{12,13}

Hao et al.⁸ reported that these aluminum hydroxides can be softer than the unsealed anodic structure. Therefore, in the following sections, a decrease in the hardness of the sealed anodic layer will be attributed to the formation of these compounds.

The XRD analysis did not detect any Ni- or F-rich precipitates, which were expected in the cold-sealed sample (see Fig. 6). This result could reasonably be produced by the insufficient amount of these precipitates, which prevented their detection by XRD. To overcome this limitation, EDS analyses were performed on the fractured cross-sections of the sealed anodic layers, and the results are shown in Fig. 7. Unlike the hydrothermal-sealed sample, the EDS spectrum after cold sealing revealed the presence of F and Ni on the anodic layer, which can be reasonably attributed to the precipitation of $\text{Ni}(\text{OH})_2$, and AlF_3 within the porous structure.¹³

Thickness of the Anodic Layer and Surface Roughness

The average thickness of the anodic layer was about $3 \pm 1 \mu\text{m}$ and $9 \pm 2 \mu\text{m}$ in the as-diecast and milled surface, respectively (see Fig. S-3 in the online supplementary material). In the as-diecast substrate, the growth of the anodic layer was mainly limited by the high eutectic fraction and the rough surface covered by numerous burrs (see Fig. S-2). Contrarily, the higher amount of α -Al phase and the smoother surface of the milled surface allowed the formation of a thicker oxide film (see in “[Characterization of the Anodic Layer](#)” section). No significant variation in the thickness of the anodic layer was observed after the sealing processes. This result agrees with previous studies, which reported how the anodic layer thickness is primarily a function of the anodizing parameters.^{2,7} However, a variation in the surface roughness parameters R_a and R_z was detected (see Fig. S-4 in the online supplementary material). Before anodizing, the as-diecast and milled substrates had mean R_a values of $0.76 \pm 0.28 \mu\text{m}$ and $0.18 \pm 0.11 \mu\text{m}$, respectively, in agreement with the typical values of surface finish for those processes.³⁵ After anodizing, the surface roughness increased, especially in the milled surface where the R_a and R_z values were more than quadrupled. A further increase in the surface roughness occurred after sealing, when, regardless of the type of sealing process, the as-diecast and milled surfaces showed R_a values of about $0.95 \pm 0.20 \mu\text{m}$ and $1.19 \pm 0.20 \mu\text{m}$, respectively. The increase of the surface roughness after the anodizing process can be explained by analyzing the growth of the oxide layer. It is important to remember that the conversion of Al into Al_2O_3 during anodizing involves a volumetric expansion. Moreover, the greater the variation in the local chemical potential from one area of the surface to another, the more pronounced is the concentration polarization effect, leading to a more inhomogeneous growth of the anodic layer.² In this study, both substrates exhibited a heterogeneous microstructure and surface irregularities (refer to Fig. S-2 and in “[Characterization of the Anodic Layer](#)” section). This resulted in significant variations in the local chemical potential of the surface, leading to a highly inhomogeneous distribution of the electrical charge during anodizing. The growth of the anodic layer was preferentially localized in certain areas of the substrate, where a greater volumetric expansion took place. The post-anodizing increase in the surface roughness was thus linked to the differential volumetric expansion between regions with varying anodic thicknesses. This effect was particularly evident in the milled

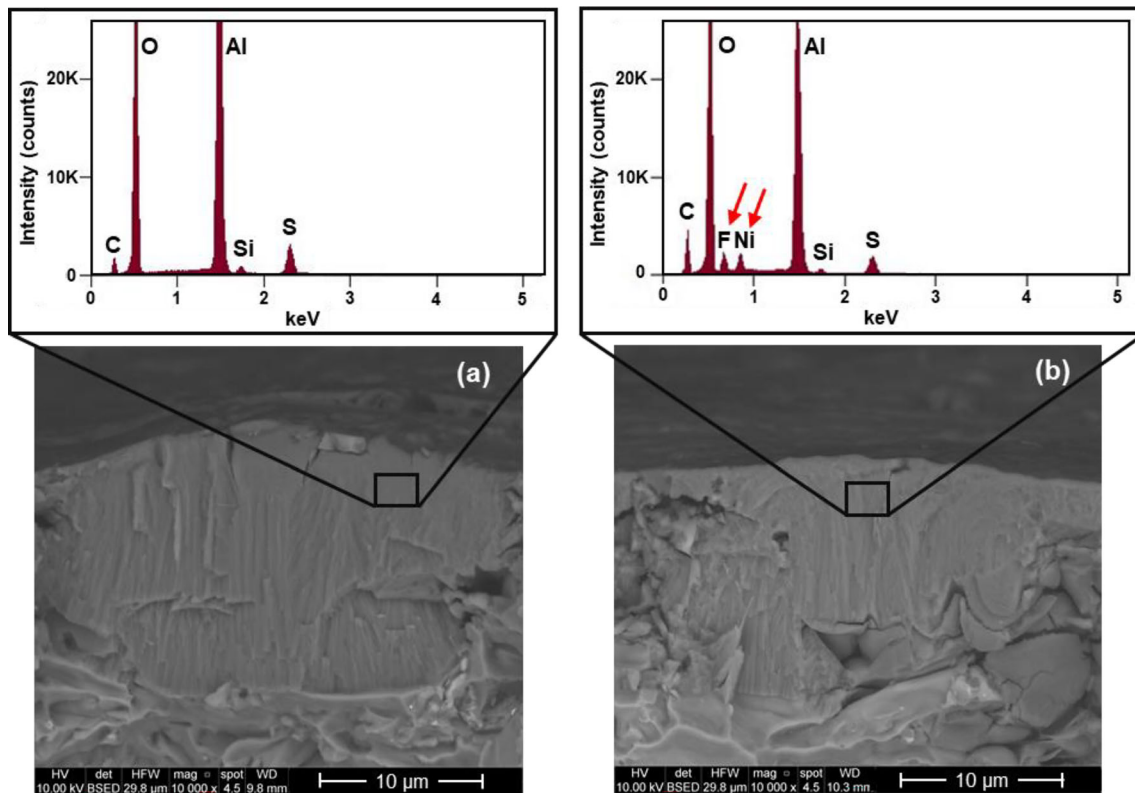


Fig. 7. FEG-SEM micrographs of the fractured cross-sections of the sealed samples. The arrows indicate the differences between the EDS spectra of the anodic layer after (a) hydrothermal sealing and (b) cold sealing.

surface, where alternating large α -Al cells and eutectic-enriched areas led to significant variations in the oxide thickness and a great increase in the surface roughness after anodizing (see Fig. 3b).

Microhardness and Scratch Results

The milled AlSi9Cu3(Fe) alloy substrate revealed a hardness of about 98 HV, which increased to about 430 HV after anodizing (see Fig. S-5 in the online supplementary material). This result agrees with the data reported in the literature.^{2,6} After cold or hydrothermal sealings, the surface microhardness slightly decreased to 409 ± 21 HV and 417 ± 17 HV, respectively, because the aluminum oxide was partially converted to softer products, i.e., bayerite and boehmite (see the discussion of Fig. 6 in “Characterization of the Anodic Layer” section).

The evolution of the scratch resistance after the different experimental conditions is shown in Fig. 8. The as-diecast substrate showed always higher scratch resistance compared to the milled one. Smooth surfaces exhibit enhanced scratch resistance compared to rougher surfaces, as demonstrated by Feng in Ref. 36. This is attributed to the absence or less frequent presence of peaks on the material surface that act as stress concentration points and can lead to the failure of the coating. In the present work, after anodizing, the as-diecast

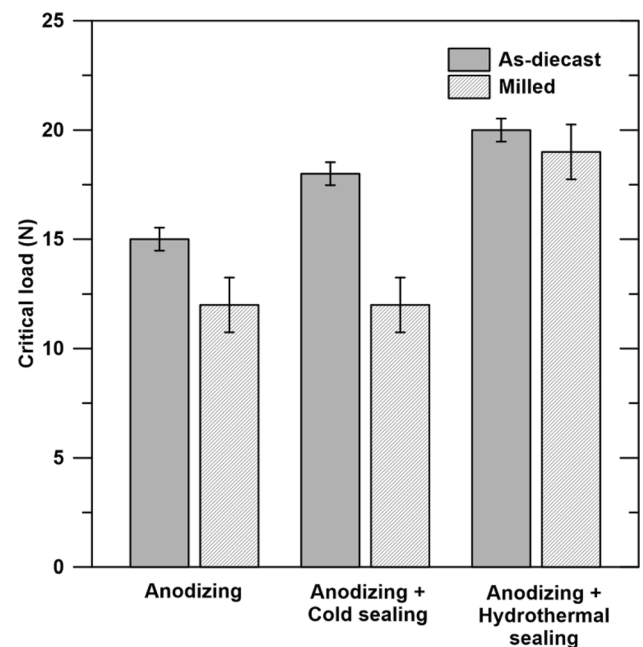


Fig. 8. Evolution of the scratch resistance after anodizing and sealing processes in the as-diecast and milled substrates. According to ISO 22557:2020 standard, the critical load corresponds to that required to scratch the oxide layer thus exposing the substrate.

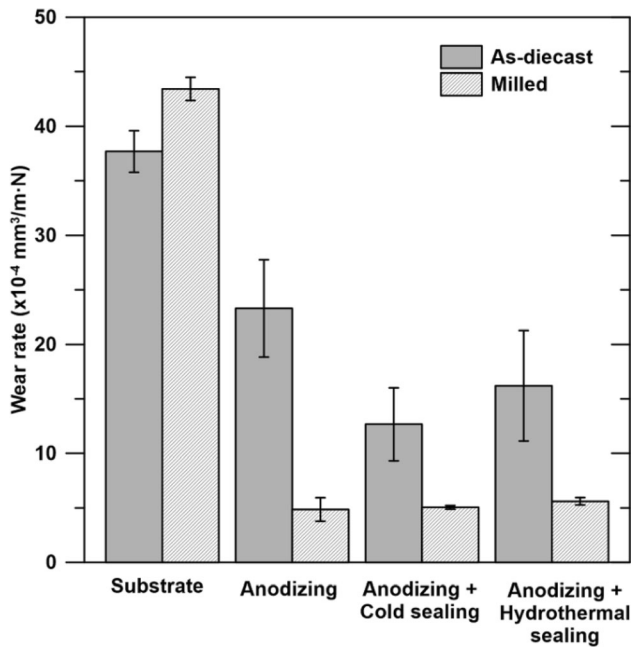


Fig. 9. Variation of the wear rate after the anodizing and sealing processes in the as-diecast and milled AlSi9Cu3(Fe) alloy substrates. The wear rates of the substrate are reported for reference.

substrate showed lower values of surface roughness compared to the milled surface (see Fig. 8), resulting in greater scratch resistance.

Especially in the milled surface, the hydrothermal process evidenced better scratch resistance than cold sealing. This behavior cannot be related to the surface roughness that was comparable after the different sealing processes (see Fig. S-4). During hydrothermal sealing, boehmite (AlO(OH)) and bayerite (Al(OH)₃) crystallized inside the porous structure (see Fig. 9), while a mixture of AlO(OH), Al(OH)₃, Ni(OH)₂, and AlF₃ precipitated inside the porous during cold sealing.¹³ Therefore, the formation of AlO(OH) and Al(OH)₃ phases within the porous structure appeared to be more effective for scratch resistance than the combined precipitation of AlO(OH), Al(OH)₃, Ni(OH)₂, and AlF₃.

Wear Behavior

The wear rate of the different experimental conditions is illustrated in Fig. 9. The as-diecast substrate showed a lower wear rate compared to the milled one because of the higher fraction of eutectic structure and intermetallic compounds (see Fig. 2). Eutectic Si particles and Fe-rich intermetallics were harder than the α -Al matrix, and they positively affected the surface wear resistance. On the other hand, the milled substrate showed larger areas of α -Al matrix, which led to a greater wear rate (see in “Characterization of the Substrate” section). It is

well known that the wear resistance is strongly related to the hardness of the material because softer surfaces show greater delamination phenomena during rolling-sliding, which significantly increase the wear rate.³⁷

After anodizing, the wear resistance of both as-diecast and milled surfaces increased because of the formation of the anodic layer, which showed higher surface hardness compared to the un-anodized substrates (Fig. 9). This effect was particularly evident in the milled substrate, where the formation of a thicker oxide layer (see Fig. 3) resulted in a greater reduction of the wear rate.

The sealing process positively affected the wear resistance of the anodic layer, especially on the as-diecast surface (Fig. 9). In particular, the cold sealing based on nickel fluoride solutions seemed to maximize the wear resistance of the anodized AlSi9Cu3(Fe) alloy. Indeed, during sealing, the voids created by the dissolution of the α -Al_x(Fe, Mn, Cr)_ySi_z phase (see Fig. 5) were partially, if not completely, sealed, forming a more compact oxide layer and increasing the wear resistance.³⁸

Figure 10 shows the representative wear tracks over the anodized and sealed surfaces. Regardless of the type of substrate, the predominant wear mechanism was adhesive wear. Evident marks of plastic deformation were observed on all the worn surfaces. Moreover, the counter body was not significantly abraded, and only adhesion phenomena of debris of aluminum or alumina on its surface were observed.

During the wear tests, the counter body initially slid on the brittle anodic layer and induced the formation of a surface tensile stress, which created wear fragments by brittle contact.³⁷ Dry air was continuously blown during the test; therefore, the fragments were easily removed from the tribological system, and the wear of the surface occurred mainly because of adhesive phenomena. However, the plowing marks detected in the wear tracks (Fig. 10b, c, and f) indicated that abrasive wear took also place as a secondary wear mechanism. When the wear fragments remained entrapped between the counter body and the sample surface, three-body abrasion phenomena occurred, and wider and deeper abrasion marks were formed inside the wear track. The tiny fragments of abraded material and the delamination marks in correspondence with the ridges formed during the milling operation are shown in Fig. 10d, e, and f.

The size of the wear tracks can be directly related to the wear rates shown in Fig. 9. The wear track formed over the as-diecast surface in the hydrothermal-sealed sample (Figs. 10b and 11a) was wider compared to the track formed on the cold-sealed sample (Figs. 10c and 11b). Similarly, the wear rate measured on the as-diecast surface in the

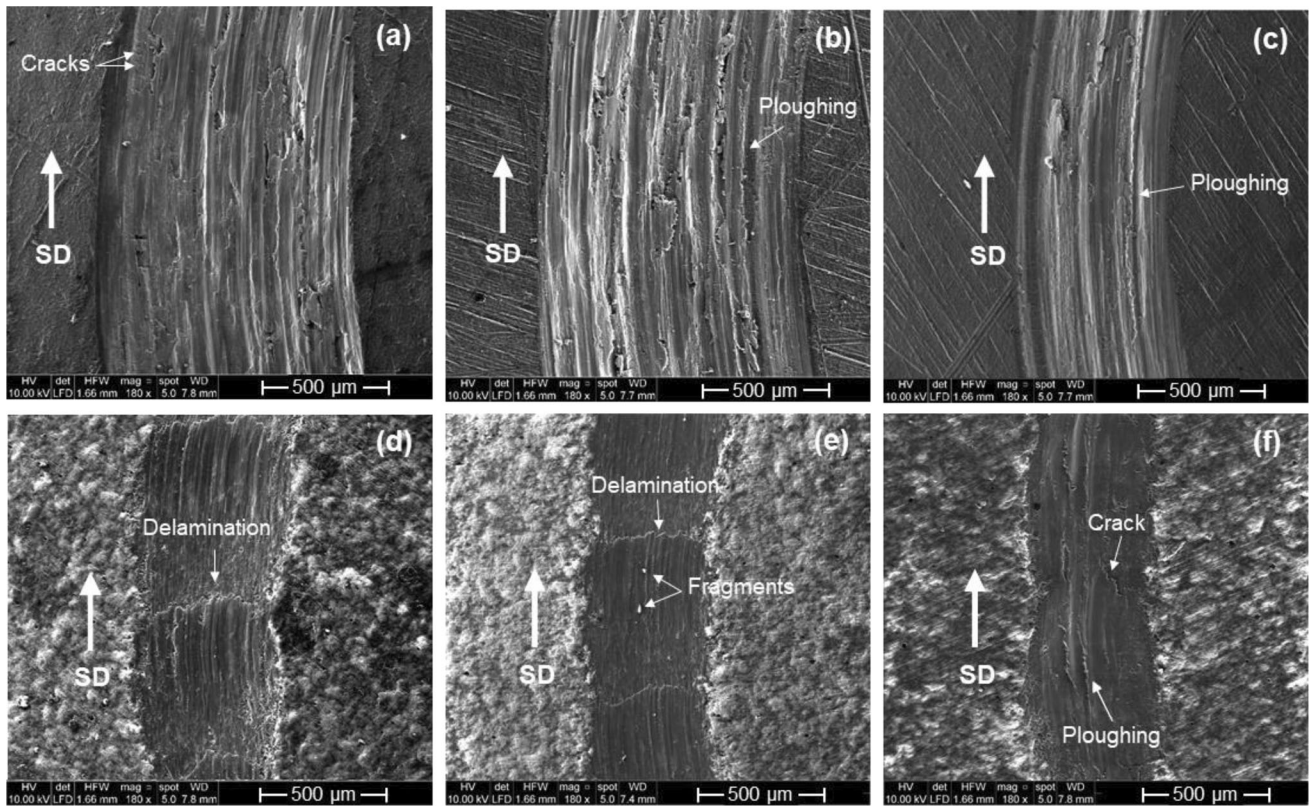


Fig. 10. Typical wear tracks of the AlSi9Cu3(Fe) alloy surfaces after (a, d) anodizing, (b, e) hydrothermal, and (c, f) cold sealings; the macrographs refer to (a–c) as-diecast and (d–f) milled substrates. The sliding direction (SD) is indicated by arrows.

hydrothermal-sealed sample was greater than the one measured in the cold-sealed one. Therefore, the analysis of the wear track confirmed the positive effect of cold sealing on the wear resistance.

Figure 11 shows the cross-section of the wear tracks formed on the as-diecast and milled surfaces after anodizing. In both cases, the aluminum substrate wore out, and extensive evidence of plastic deformation was detected in the regions close to the contact zone (Fig. 11c and d). The sliding tangential stresses developed during the tribological testing led to the fragmentation of the intermetallic compounds and to their incorporation in the mechanically mixed layer (MML), as shown in Fig. 11e. The intense stresses also caused the cracking of the MML, as evidenced by the formation of numerous cracks parallel to the surface (Fig. 11c and d). Sulfur-rich zones were also detected in the EDS mapping of the mechanically mixed layer, indicating that debris of the anodic layer was also incorporated in the MML (Fig. 11g). Due to the most severe wear of the aluminum substrate, the MML formed on the as-diecast surface showed lower sulfur content compared to the MML on the milled surface.

Figure 12 shows the evolutions of the friction coefficient in the as-diecast surface at the different experimental conditions as a function of the sliding distance during the wear test. The friction coefficients measured on the milled substrates showed similar variations. Two main regions can be identified in the trend of the friction coefficient, i.e., an initial run-in and a following steady-state condition. In the first phase, the Al₂O₃ ball entered into contact with the sample surface. As the sliding distance increased, a greater amount of abraded aluminum or alumina debris was transferred from the sample surface to the counter body, and the value of the friction coefficient gradually increased. In the un-anodized surfaces, this period was quite short because the debris of the alloy substrate was easily transferred from the surface to the counter body because of the high plasticity of the α -Al matrix. Contrarily, longer times were necessary for the anodized sample to reach the steady-state condition because the anodic layer was harder than the Al alloy substrate and was usually worn by creating wear fragments by brittle contact. The second phase, corresponding to the steady-state condition, started when the surface of the counter body was covered by a layer of transferring debris.

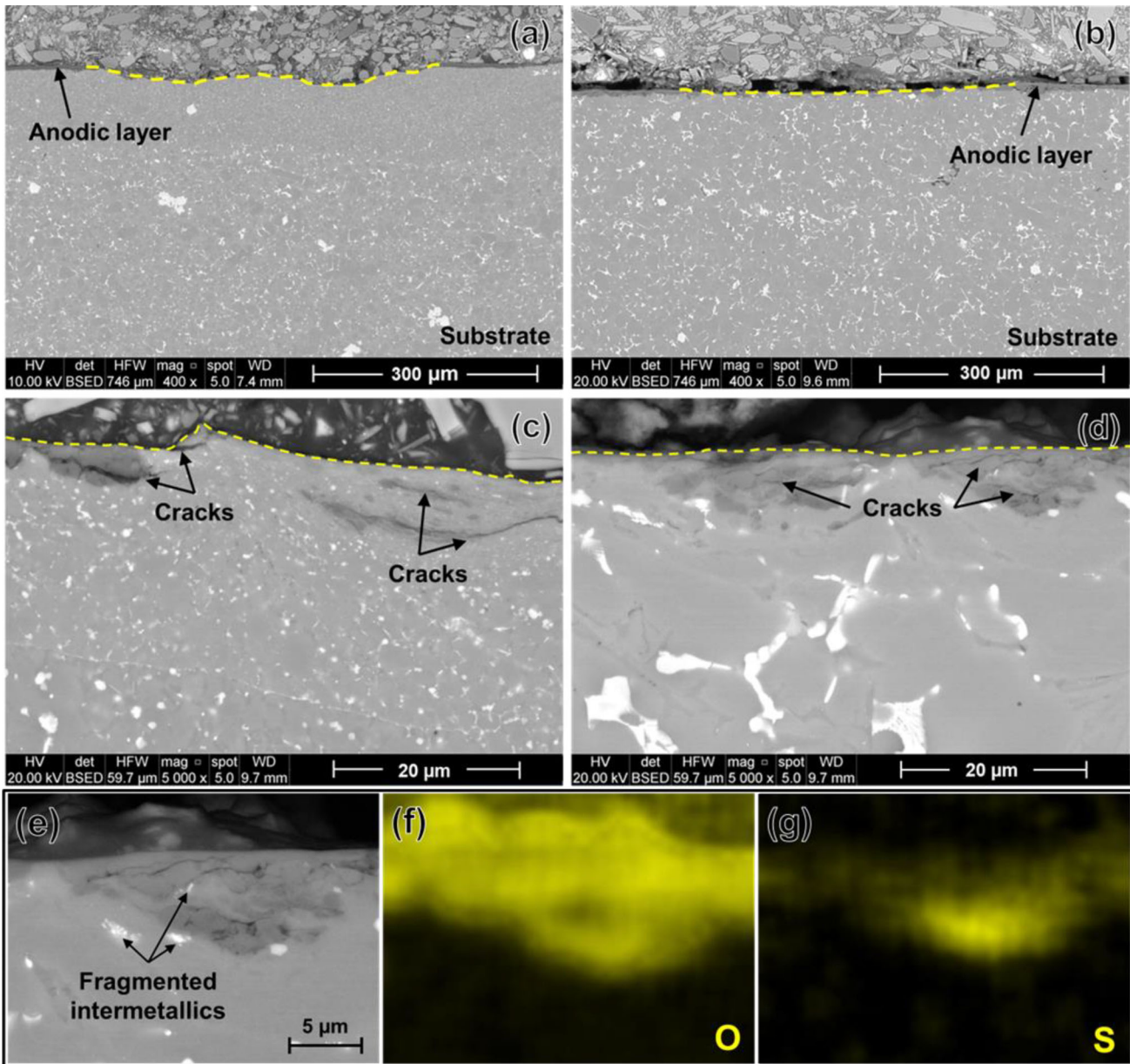


Fig. 11. Cross-section micrographs at increasing magnifications of the wear tracks formed on the (a, c) as-diecast and (b, d, e) milled substrates. The dotted yellow lines show the profile of the wear track. (e) FEG-SEM micrograph and (f, g) EDS mapping showing the distribution of oxygen and sulfur in the mechanically mixed layer (Color figure online).

In this phase, the values of the friction coefficient were stabilized around a mean value of 0.5 in all the experimental conditions. During this period, no differences were detected between the un-anodized and the anodized samples.

CONCLUSION

The effects of the sealing processes on the wear and scratch resistance of a diecast AlSi9Cu3(Fe) alloy were investigated. As-diecast and milled surfaces were studied after hydrothermal sealing and cold sealing based on a nickel fluoride solution. The following conclusions can be drawn:

- The sealing process had no significant effect on the thickness and surface roughness of the anodic layer. However, it positively affected its scratch and wear resistance by sealing the surface porosity, which was formed during anodizing due to the dissolution of the $\alpha\text{-Al}_x(\text{Fe,Mn,Cr})_y\text{Si}_z$ phase.
- The hydrothermal sealing maximized the scratch resistance of the anodic layer both in as-diecast and milled surfaces.
- After anodizing, milled surfaces showed greater wear resistance compared to as-diecast ones because of the presence of a thick anodic layer that limited the severe wear of the underlying

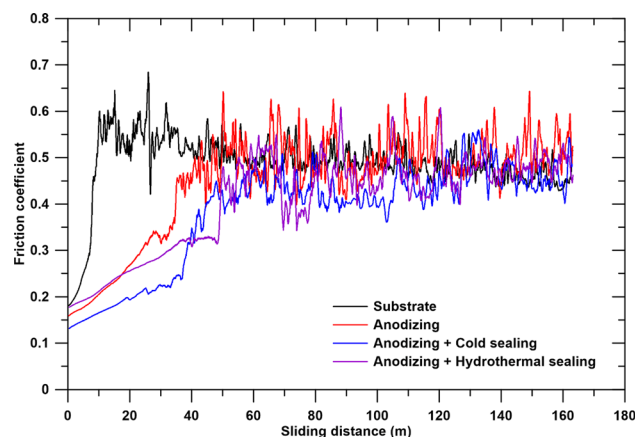


Fig. 12. Variation of the friction coefficient as a function of the sliding distance on the as-diecast surface.

aluminum substrate.

- The mechanically mixed layer formed on anodized surfaces was distinguished by the presence of numerous cracks parallel to the surface, fragmented intermetallic compounds, and anodic layer debris.
- Concerning the as-diecast surface, the friction coefficient showed the lowest values in the initial run-in after cold sealing, resulting in increased wear resistance.

SUPPLEMENTARY INFORMATION

The online version contains supplementary material available at <https://doi.org/10.1007/s11837-023-06241-3>.

ACKNOWLEDGEMENTS

The work was developed with the financial support of Fondazione Cassa di Risparmio di Padova e Rovigo (CaRiPaRo).

FUNDING

Open access funding provided by Università degli Studi di Padova.

CONFLICT OF INTEREST

On behalf of all authors, the corresponding author states that there is no conflict of interest.

ETHICAL APPROVAL

This article does not contain any studies with human participants or animals performed by any of the authors.

OPEN ACCESS

This article is licensed under a Creative Commons Attribution 4.0 International License, which permits use, sharing, adaptation, distribution and reproduction in any medium or format, as long as you give appropriate credit to the original author(s) and the source, provide a link to the Creative Commons licence, and indicate if changes were made. The images or other third party material in this article are included in the article's Creative Commons licence, unless indicated otherwise in a credit line to the material. If material is not included in the article's Creative Commons licence and your intended use is not permitted by statutory regulation or exceeds the permitted use, you will need to obtain permission directly from the copyright holder. To view a copy of this licence, visit <http://creativecommons.org/licenses/by/4.0/>.

REFERENCES

1. F.C.R. Hernandez, J.M.H. Ramirez, and R. Mackay, *Al-Si Alloys: Automotive, Aeronautical, and Aerospace Applications* (Springer, Cham, 2017), pp1–3.
2. J.M. Runge, *The Metallurgy of Anodizing Aluminum* (Springer, Cham, 2018), pp. 149–154, 158–159, 269–274.
3. J.M. Runge and L. Chesterfield, *Alum. Int. Today* 22, 25 (2010).
4. P. Atz-Dick, A. Konrath, Y. Rátiva Melo, C. Radtke, and L.F.P. Dick, *Appl. Surf. Sci.* 593, 153392 (2022).
5. E. Dervishi, M. McBride, R. Edwards, M. Gutierrez, N. Li, R. Buntyn, and D.E. Hooks, *Surf. Coat. Technol.* 444, 128652 (2022).
6. ASM International Handbook Committee, in *ASM Metals Handbook—Surface Engineering*, vol 5. ed. by F. Reidenbach (ASM International, Russell, 1994), pp. 1416–1431.
7. G. Scampone, and G. Timelli, *Adv. Eng. Mater.* 24, 2101480 (2022).
8. L. Hao and B. Rachel Cheng, *Met. Finish.* 98, 8 (2000).
9. A. Carangelo, M. Curioni, A. Acquesta, T. Monetta, and F. Bellucci, *J. Electrochem. Soc.* 163, C619 (2016).
10. Y. Zuo, P.H. Zhao, and J.M. Mao, *Surf. Coat. Technol.* 166, 237 (2003).
11. S.U. Ofoegbu, F.A.O. Fernandes, and A.B. Pereira, *Coatings* 10, 226 (2020).
12. S. Ono and H. Asoh, *Corros. Sci.* 181, 109221 (2021).
13. V. López, M.J. Bartolomé, E. Escudero, E. Otero, and J.A. González, *J. Electrochem. Soc.* 153, B75 (2006).
14. P.L. Cavallotti, L. Nobili, D. Piconi, and E. Galbiati, *Trans. IMF* 68, 38 (1990).
15. M.R. Kalantary, D.R. Gabe, and D.H. Ross, *J. Appl. Electrochem.* 22, 268 (1992).
16. T.Z.Y. Xuan and W.W.L. Zhang, *Sealing Agent for Aluminum and Aluminum Alloy Anode Oxide Films and Preparation Method for Sealing Agent*, CN102650068B (Google Patents, 2012). [https://patents.google.com/patent/CN102650068B/en?q=Y.+Xuan%2c+and+W.+W.+L.+Zhang%2c+CN102650068B+\(2012\)](https://patents.google.com/patent/CN102650068B/en?q=Y.+Xuan%2c+and+W.+W.+L.+Zhang%2c+CN102650068B+(2012)). Accessed 10 June 2022.
17. D. Zhang, J. Zhang, and G. Mao, *Metal Salt-Free Sealing Agent for Aluminum Alloy Anodic Oxide Film*, CN101864589B (Google Patents, 2010). [https://patents.google.com/patent/CN101864589B/en?q=17.D.+Zhang%2c+J.+Zhang%2c+and+G.+Mao%2c+CN101864589B+\(2010\)](https://patents.google.com/patent/CN101864589B/en?q=17.D.+Zhang%2c+J.+Zhang%2c+and+G.+Mao%2c+CN101864589B+(2010)). Accessed 10 June 2022.
18. P. Lu, C. Gao, and X. Cui, *Sealing Reagent for Aluminum Alloy*, EP2350356B1 (Google Patents, 2008). <https://patents.google.com/patent/EP2350356B1/de?q=EP2350356B1>. Accessed 10 June 2022.

19. Z. Yu, C. Xing, J. Li, and A. Jankowski, *Anodization Sealing Process for an Aluminum or Aluminum Alloy Element for Vehicles*, US9771663B2 (Google Patents, 2017). <https://patents.google.com/patent/US9771663B2/en?q=Yu%2c+Xing%2c+J.+Li%2c+and+A.+Jankowski%2c+US9771663B2>. Accessed 10 June 2022.
20. M. Mohedano, E. Matykina, R. Arrabal, B. Mingo, and A. Pardo, *Appl. Surf. Sci.* 346, 57 (2015).
21. B. Zhu, *Casting and Anodizing of Al Alloys—Alloy Design, Manufacturing Process and Material Properties* (Jönköping University, 2019), pp. 17, 23–26, 41–46.
22. British Standards Institution (BSI), *Aluminium and Aluminium Alloys—Castings—Chemical Composition and Mechanical Properties*, Standard No. EN 1706:2020 (BSI Standards Publication, London, 2020).
23. S. Ferraro, G. Timelli, and A. Fabrizi, *Mater. Sci. Forum* 765, 59 (2013).
24. G. Timelli and A. Fabrizi, *Metall. Mater. Trans. A Phys. Metall. Mater. Sci.* 45, 5486 (2014).
25. C.M. Gourlay, H.I. Laukli, and A.K. Dahle, *Metall. Mater. Trans. A Phys. Metall. Mater. Sci.* 38, 1833 (2007).
26. ASM International Handbook Committee, in *Aluminum and Aluminum Alloys*. ed. by J.R. Davis (ASM International, Russell, 1993), pp. 614–615.
27. E. Vandersluis and C. Ravindran, *Metallogr. Microstruct. Anal.* 6, 89 (2017).
28. British Standards Institution, *Paints and Varnishes—Scratch Test Using a Spring-Loaded Pen*, Standard No. EN ISO 22557:2020 (BSI Standards Publication, London, 2020).
29. D. Caliari, G. Timelli, B. Zabala, and A. Igartua, *Surf. Coat. Technol.* 352, 462 (2018).
30. B. Zhu, S. Seifeddine, A.E.W. Jarfors, P. Leisner, and C. Zanella, *Solid State Phenom.* 285, 39 (2019).
31. L.E. Fratila-Apachitei, H. Terry, P. Skeldon, G.E. Thompson, J. Duszczyk, and L. Katgerman, *Electrochim. Acta* 49, 1127 (2004).
32. B. Zhu and C. Zanella, *Surf. Coat. Technol.* 422, 127570 (2021).
33. M.S. Ilango, A. Mutalikdesai, and S.K. Ramasesha, *J. Chem. Sci.* 128, 153 (2016).
34. J. Lee, Y. Kim, J. Kim, and W. Chung, *J. Nanoelectron. Optoelectron.* 9, 136 (2014).
35. W. Grzesik, B. Kruszynski, and A. Ruszaj, in *Surface Integrity in Machining*. ed. by J. Paulo Davim (Springer, Cham, 2010), p. 147.
36. B. Feng, *AIP Adv.* 7, 035217 (2017).
37. G. Straffelini, *Friction and Wear: Methodologies for Design and Control* (Springer, Cham, 2015), pp. 84–90.
38. A.L. Yerokhin, X. Nie, A. Leyland, A. Matthews, and S.J. Doney, *Surf. Coat. Technol.* 122, 73 (1999).

Publisher's Note Springer Nature remains neutral with regard to jurisdictional claims in published maps and institutional affiliations.